Lepton collider imprints of an inelastic dark matter model

Wei Liu[1] and Jin Sun[2,*]

[1]*Department of Applied Physics and MIIT Key Laboratory of Semiconductor Microstructure and Quantum Sensing, Nanjing University of Science and Technology, Nanjing 210094, China*
[2]*Particle Theory and Cosmology Group, Center for Theoretical Physics of the Universe, Institute for Basic Science (IBS), Daejeon 34126, Korea*

(Received 2 April 2025; accepted 1 June 2025; published 20 June 2025)

We explore the potential for detecting the inelastic dark matter (DM) model with an additional $U(1)_D$ gauge symmetry at various types of lepton colliders. The new gauge boson Z' resulting from the spontaneous breaking of $U(1)_D$ can act as a portal connecting the Standard Model fermions and DM fermions χ, thereby facilitating the production of Z' and its decay into DM fermions. The mass difference between the excited DM fermion χ_2 and the ground DM fermion χ_1 induces the subsequent decays $\chi_2 \to \chi_1 + \text{vis}$, where χ_2 and χ_1 serve as long-lived particles and the DM candidate, respectively. For the inelastic DM with a mass m_{χ_1} in the range of (1–100) GeV, we find that the future lepton colliders can probe many regions not accessible by current experiments and provide greater projected sensitivity than the LHC and Belle in previous studies. This suggests that future colliders can provide complementary exploration of the inelastic dark matter model.

DOI: 10.1103/4ght-wb9f

I. INTRODUCTION

Although direct detection remains elusive, cosmological observations and early Universe simulations provide indirect evidence for the presence of dark matter (DM), which is believed to constitute approximately 85% of the total matter [1,2]. Nonetheless, fundamental questions remain unresolved, such as the microscopic nature of DM and the origin of its observed relic density. Numerous dark-sector models have been proposed to explain the nature of DM, including gauge bosons, scalar bosons, and fermions; see, e.g., [3–5] for reviews. In this framework, it is hypothesized that there exists a new sector of particles below the electroweak scale that are neutral under the Standard Model (SM) but could exhibit observable phenomena.

DM detection and identification at the microscopic level primarily involve direct detection, indirect detection, and collider experiments. The first two types of searches rely on observing recoils from the elastic scattering of DM particles on the nuclei in the detector material or detecting annihilation products of DM pairs, such as monochromatic photons. Collider searches for DM, on the other hand, rely on the production of DM particles in high-energy particle collisions and can be divided into two broad categories based on the experimental signatures they produce: (i) searches for missing transverse momentum plus X signatures for triggering, and (ii) searches involving only visible particles, such as pairs of leptons or jets, aimed at detecting the particles mediating interactions between DM and SM particles through the observation of new resonances or modifications in the kinematics of the final-state particles.

Among various DM models, the inelastic DM (iDM) model has attracted significant attention, originally motivated by the explanation of the DAMA excess [6]. A straightforward realization of the iDM scenario is that the DM particle charged under a hidden gauge or global symmetry experiences spontaneous symmetry breaking, resulting in symmetry-breaking masses much smaller than the symmetry-preserving ones, thus generating off-diagonal DM interactions. Therefore, the particle components of the iDM scenario include the dark photon Z' from the global $U(1)_D$ symmetry, a scalar Φ responsible for $U(1)$ breaking to give the mass $m_{Z'}$, and new dark fermions χ_1 and χ_2, with the ground state χ_1 serving as the DM candidate and χ_2 as a long-lived particle. Given the relatively long lifetime of χ_2, a common method called the displaced vertex technique is used to detect long-lived particles via signatures [7–12]. Further extensive studies and search strategies for the iDM model can be found in Refs. [13–30], achieving sensitivity to the kinetic mixing $\epsilon \sim 10^{-3}$ around the inelastic DM mass range

*Contact author: sunjin0810@ibs.re.kr

Published by the American Physical Society under the terms of the Creative Commons Attribution 4.0 International license. Further distribution of this work must maintain attribution to the author(s) and the published article's title, journal citation, and DOI. Funded by SCOAP³.

(1–100) GeV. Here, ϵ denotes the kinetic mixing strength between the new $U(1)_D$ gauge field X and the $U(1)_Y$ hypercharge field B represented as $\epsilon/2X_{\mu\nu}B^{\mu\nu}$. Note that the above investigations are primarily based on the hadron colliders LHC and Belle. Given the advantages of lepton colliders (clean environment, fixed collider energy, higher luminosity, etc.), they may provide much greater sensitivity to ϵ, warranting further detailed exploration. To the best of our knowledge, no relevant research has been conducted in this particular direction to date, except for a similar study involving exotic Z-boson decays in the context of magnetic inelastic dark matter [31]. Since χ_1 serves as the DM candidate required by the observed DM relic density, we focus on the mass range $m_{\chi_1} \in (1, 100)$ GeV [13,14,19].

In this paper, we investigate the potential of lepton colliders to probe the iDM model with an additional $U(1)_D$ gauge symmetry. The new gauge boson Z' acts as a portal connecting the visible electrons and the dark states $\chi_{1,2}$, facilitating the production of DM fermions.[1] Moreover, the mass splitting between the two dark states ($\Delta_\chi = m_{\chi_2} - m_{\chi_1}$) induced by the interaction between the dark Higgs field and the DM sector leads to the decay of the excited state χ_2 into the ground state χ_1.

The rest of the paper is organized as follows: In Sec. II, we discuss the details of the iDM model with a $U(1)_D$ gauge symmetry. Section III presents the collider signatures at different e^+e^- colliders. In Sec. IV, we present our results on the sensitivity to the iDM model parameters from different lepton colliders. We provide our conclusions in Sec. V.

II. INELASTIC DARK MATTER MODEL

In this section, we briefly review the inelastic dark matter models with a $U(1)_D$ gauge symmetry, focusing on fermionic DM candidates. The gauge group of the model is $SU(3)_C \times SU(2)_L \times U(1)_Y \times U(1)_D$. In addition to the SM particles, new particles are introduced: a singlet complex scalar field Φ and a Dirac fermion field χ, as shown in Table I. All SM particles are neutral under the $U(1)_D$ symmetry and cannot couple directly to the dark sector. Note that the $U(1)_D$ gauge symmetry is broken into its Z_2 subgroup, with Z_2-odd DM candidate χ, to ensure the DM stability. The relevant particles and their charges are shown in Table I.

The relevant gauge invariant and renormalizable Lagrangian can be written as [30]

TABLE I. The model particles and corresponding charges.

	SM particles	Singlet scalar Φ	Dirac fermion χ
$U(1)_D$	0	+2	+1
Z_2	+1	+1	−1

$$\begin{aligned}\mathcal{L} = \mathcal{L}_{\rm SM} &- \frac{1}{4}X_{\mu\nu}X^{\mu\nu} - \frac{1}{2}\epsilon X_{\mu\nu}B^{\mu\nu} + \mathcal{D}^\mu\Phi^\dagger\mathcal{D}_\mu\Phi \\ &- \mu_\Phi^2\Phi^\dagger\Phi - \lambda_\Phi(\Phi^\dagger\Phi)^2 - \lambda_{\mathcal{H}\Phi}\mathcal{H}^\dagger\mathcal{H}\Phi^\dagger\Phi \\ &+ \bar{\chi}(i\not{\mathcal{D}} - M_\chi)\chi - \left(\frac{\xi}{2}\Phi^\dagger\overline{\chi^c}\chi + \text{H.c.}\right). \end{aligned} \tag{1}$$

Here the first line in Eq. (1) refers to the kinetic energy terms involving the $X_{\mu\nu}(B_{\mu\nu})$ field strength tensors of $U(1)_D(U(1)_Y)$ gauge fields. ϵ is the kinetic mixing, quantifying the Abelian mixing strength between $X_{\mu\nu}$ and $B_{\mu\nu}$.

The second line in Eq. (1) describes the scalar potential composed by complex doublet H and singlet Φ as

$$\begin{aligned} H &= \begin{pmatrix} h^+ \\ \frac{1}{\sqrt{2}}(v + h + iA) \end{pmatrix}, \\ \Phi &= \frac{1}{\sqrt{2}}(v_X + h_X + iA_X), \end{aligned} \tag{2}$$

where $v(v_X)$ are vacuum expectation values of $H(\Phi)$, which are responsible for breaking the electroweak $[U(1)_D]$ symmetries, respectively, and $v = 246$ GeV. After symmetry breaking, the two scalar fields will mix with each other to generate the physical fields as

$$\begin{pmatrix} h \\ h_X \end{pmatrix} = \begin{pmatrix} c_\alpha & s_\alpha \\ -s_\alpha & c_\alpha \end{pmatrix}\begin{pmatrix} H_1 \\ H_2 \end{pmatrix}, \qquad \sin 2\alpha = \frac{\lambda_{H\Phi} v v_X}{m_{H_2}^2 - m_{H_1}^2}; \tag{3}$$

here, $c_\alpha = \cos\alpha$, $s_\alpha = \sin\alpha$. In the following analysis, we adopt the same notation. We identify H_1 as the observed SM-like Higgs with $m_{H_1} = 125$ GeV.

The third line in Eq. (1) describes the fermion interaction relevant to new Dirac fermion χ, which is further decomposed into two Majorana fermion fields $\chi_{1,2}$ as

$$\chi = \frac{1}{\sqrt{2}}(\chi_2 + i\chi_1), \qquad \chi_2 = \chi_2^c, \qquad \chi_1 = \chi_1^c. \tag{4}$$

After the $U(1)_D$ symmetry breaking, the DM interaction can be expanded as

[1]The possibility of Z' decays into right-handed neutrinos has also raised a lot of attention [32–42].

$$\mathcal{L}_\chi = \frac{1}{2}\sum_{n=1,2}\overline{\chi_n}(i\partial\!\!\!/ - M_\chi)\chi_n - i\frac{g_D}{2}(\overline{\chi_2}X\!\!\!/\chi_1 - \overline{\chi_1}X\!\!\!/\chi_2) - \frac{\xi}{2\sqrt{2}}(v_X + h_X)(\overline{\chi_2}\chi_2 - \overline{\chi_1}\chi_1). \quad (5)$$

Furthermore, we obtain the $\chi_{1,2}$ mass as

$$M_{\chi_{1,2}} = M_\chi \mp \frac{1}{\sqrt{2}}\xi v_X, \quad (6)$$

with the mass splitting parametrized as

$$\Delta_\chi = \sqrt{2}\xi v_X. \quad (7)$$

Generally, the kinetic mixing $\epsilon X_{\mu\nu}B^{\mu\nu}$ in Eq. (1) can be removed by different ways: (a) X_p in the canonical form does not couple to hypercharge current j_Y^μ [43,44]; (b) the hypercharge field in the canonical form B_p does not couple to dark current j_X^μ [45,46]; (c) in the most general scenario, an orthogonal transformation can be used such that, in the canonical basis, both the dark gauge boson X_p and the hypercharge gauge field B_p couple to j_Y^μ and j_X^μ [47]. Here we choose case (b) to conduct the analysis with the following transformation as [48]

$$\begin{pmatrix} B \\ X \end{pmatrix} = \begin{pmatrix} 1 & -\eta \\ 0 & \frac{1}{\sqrt{1-\epsilon^2}} \end{pmatrix}\begin{pmatrix} B_p \\ X_p \end{pmatrix}; \quad (8)$$

here we define $\eta = \epsilon/\sqrt{1-\epsilon^2}$.

The mass terms of gauge bosons are from the scalar kinetic term given by

$$\mathcal{L}_{\text{scalar}} = D^\mu\Phi^+ D_\mu\Phi + D^\mu H^+ D_\mu H \quad \text{with} \quad D_\mu = (\partial_\mu + ig'YB_\mu + igT_i W_{i\mu} + ig_D Q_X X_\mu). \quad (9)$$

Here, g', g, and g_D are the $U(1)_Y$, $SU(2)_L$, and $U(1)_D$ gauge coupling constants, respectively. Similarly, we need to adopt the transformation in Eq. (8) to express the fields in the canonical form B_p and X_p. After electroweak symmetry breaking, we have

$$B_{p\mu} = c_W\tilde{A}_\mu - s_W\tilde{Z}_\mu, \qquad W_\mu^3 = s_W\tilde{A}_\mu + c_W\tilde{Z}_\mu, \quad (10)$$

where θ_W is the weak mixing angle. Moreover, the $\tilde{Z}$ and X_p fields both receive the mass as

$$\mathcal{L}_{\text{mass}} = \frac{1}{2}(\tilde{Z}^\mu, X_p^\mu)M^2\begin{pmatrix} \tilde{Z}_\mu \\ X_{p\mu} \end{pmatrix}, \quad (11)$$

with the corresponding mass squared matrix element as

$$M^2 = m_{\tilde{Z}}^2\begin{pmatrix} 1 & s_W\eta \\ s_W\eta & \Delta_Z + \eta^2 s_W^2 \end{pmatrix}. \quad (12)$$

Here $m_{\tilde{Z}}^2 = g_Z^2 v^2/4$, $m_{X_p}^2 = 4g_D^2 v_X^2$ with $g_Z = \sqrt{g'^2 + g^2}$ and $\Delta_Z = m_{X_p}^2/m_{\tilde{Z}}^2$.

In order to obtain the mass matrix in the physical basis, we need further diagonalize the mass matrix in Eq. (12) by introducing the mixing angle as

$$\begin{pmatrix} Z \\ Z' \end{pmatrix} = \begin{pmatrix} c_\theta & s_\theta \\ -s_\theta & c_\theta \end{pmatrix}\begin{pmatrix} \tilde{Z} \\ X_p \end{pmatrix} \quad \text{with} \quad \tan(2\theta) = \frac{2\eta s_W}{1 - \Delta_Z - \eta^2 s_W^2} \approx \frac{2\epsilon s_W}{1-\Delta_Z}. \quad (13)$$

The diagonal masses m_Z^2 and $m_{Z'}^2$ are given by

$$m_Z^2 = m_{\tilde{Z}}^2[c_\theta^2 + (\Delta_Z + \eta^2 s_W^2)s_\theta^2 + 2s_\theta c_\theta s_W\eta],$$
$$m_{Z'}^2 = m_{\tilde{Z}}^2[s_\theta^2 + (\Delta_Z + \eta^2 s_W^2)c_\theta^2 - 2s_\theta c_\theta s_W\eta]. \quad (14)$$

Because of the assumption $\epsilon \ll 1$, $m_{Z'} \approx m_{X_p} = 2g_D v_X$.

Combining the all transformations in Eqs. (8), (10), and (13), we obtain the resulting form as

$$\begin{pmatrix} A_p \\ \tilde{Z} \\ X \end{pmatrix} = \begin{pmatrix} 1 & -s_\theta c_W\eta & -c_\theta c_W\eta \\ 0 & c_\theta + s_\theta s_W\eta & -s_\theta + c_\theta s_W\eta \\ 0 & s_\theta\frac{1}{\sqrt{1-\epsilon^2}} & c_\theta\frac{1}{\sqrt{1-\epsilon^2}} \end{pmatrix}\begin{pmatrix} A \\ Z \\ Z' \end{pmatrix}. \quad (15)$$

Here, A_p is the original photon component resulting from the mixing of hypercharge field B and W^3 under the condition of $\epsilon = 0$.

The general Lagrangian that describes the physical fields (A, Z, Z') kinetic energy and their interactions with the electromagnetic current j_{em}^μ, neutral Z-boson current j_Z^μ, and dark current j_X^μ is given by

$$\mathcal{L} = -\frac{1}{4}Z'_{\mu\nu}Z'^{\mu\nu} - \frac{1}{4}A_{\mu\nu}A^{\mu\nu} - \frac{1}{4}Z_{\mu\nu}Z^{\mu\nu} + j_{em}^\mu(A_\mu - s_\theta c_W\eta Z_\mu - c_\theta c_W\eta Z'_\mu) + j_Z^\mu[(c_\theta + s_\theta s_W\eta)Z_\mu + (-s_\theta + c_\theta s_W\eta)Z'_\mu] + j_{Z'}^\mu\left(s_\theta\frac{1}{\sqrt{1-\epsilon^2}}Z_\mu + c_\theta\frac{1}{\sqrt{1-\epsilon^2}}Z'_\mu\right). \quad (16)$$

Here the currents for fermions with charge Q_f and weak isospin I_3^f in the SM are given by

$$j^{\mu}_{em} = -\sum_f eQ_f \bar{f}\gamma^{\mu} f,$$
$$j^{\mu}_{Z} = -\frac{e}{2s_W c_W}\bar{f}\gamma^{\mu}(\tilde{g}^f_V - \tilde{g}^f_A\gamma_5)f,$$
$$j^{\mu}_{Z'} = -i\frac{g_D}{2}(\overline{\chi_2}\gamma^{\mu}\chi_1 - \overline{\chi_1}\gamma^{\mu}\chi_2); \quad (17)$$

here, $\tilde{g}^f_V = I^f_3 - 2Q_f s^2_W$ and $\tilde{g}^f_A = I^f_3$.

For the linear order approximation in ϵ, Z' interacts with SM fermions as

$$\mathcal{L}_{Z'\bar{f}f} = e\epsilon\bar{f}\gamma^{\mu}(c^f_V + c^f_A\gamma_5)fZ'_{\mu},$$
$$c^f_V = c_W Q_f + \frac{\tilde{g}^f_V}{2c_W}\frac{\Delta_Z}{1-\Delta_Z}, \quad c^f_A = \frac{-\tilde{g}^f_A}{2c_W}\frac{\Delta_Z}{1-\Delta_Z}. \quad (18)$$

The first term in c_V originates from the electromagnetic current j_{em}, while the remaining terms come from the Z-boson current j_Z. In fact, the terms from j_Z play an important role in the production of the new gauge boson Z', especially for large mass $m_{Z'}$ or around m_Z, which have usually been neglected in previous studies [25,30].

Before performing the detailed collider analysis, we first analyze the relevant decay processes for the new gauge boson Z' and the excited dark fermion χ_2. For the gauge boson Z', it can interact with the SM fermion in Eq. (18) and dark fermion in Eq. (5). We calculate the corresponding decay width as follows:

$$\Gamma(Z' \to f\bar{f}) = \frac{\alpha_{em}\epsilon^2}{3}m_{Z'}\sqrt{1-\frac{4m^2_f}{m^2_{Z'}}}[(c^f_V)^2 + (c^f_A)^2],$$
$$\Gamma(Z' \to \chi_1\chi_2) = \frac{m_{Z'}}{12\pi}g^2_D\lambda\left(1, \frac{m^2_{\chi_1}}{m^2_{Z'}}, \frac{m^2_{\chi_2}}{m^2_{Z'}}\right). \quad (19)$$

Here, $\lambda(x,y,z) = x^2 + y^2 + z^2 - 2xy - 2xz - 2yz$, and α_{em} is the fine structure constant. $f = q, l, \nu$ represents the SM fermions if the decay is kinematically allowed. Based on the above formula, we plot the relevant Z' decay branching ratios as shown in Fig. 1(a). Here we choose the benchmark points: $m_{\chi_1} = 10\Delta_\chi = m_{Z'}/3$, $\alpha_D = 0.1$, and $\epsilon = 0.1$. We find that the dominant decay channel is $\mathrm{Br}(Z' \to \chi_1\chi_2) \sim 1$. The only exception occurs around $m_{\chi_1} \sim 30$ GeV, where it lies at the pole $\Delta_Z \sim 1$ in Eq. (18), with the enhanced Z' interactions with SM fermions. If choosing a much smaller kinetic mixing $\epsilon \sim 10^{-3}$, $(Z' \to \chi_2\chi_1)$ becomes the dominant decay chain across all Z' mass regions.

For χ_2, its decay chains are $\chi_2 \to \chi_1 +$ SM mediated by Z' via Eqs. (5) and (18). The SM particles can include a pair of jets, charged leptons, and neutrinos. In the approximation $m_{Z'} \gg \Delta_\chi \gg m_l$, we can obtain the partial decay width $\chi_2 \to \chi_1 ll$ as

$$\Gamma(\chi_2 \to \chi_1 ll) = \frac{4\alpha_D\alpha_{em}\Delta^5_\chi\epsilon^2}{9\pi m^4_{Z'}}c^2_W \times\left[\left(1 - \frac{\tilde{g}^l_V}{2c^2_W}\frac{\Delta_Z}{1-\Delta_Z}\right)^2 + \left(\frac{\tilde{g}^l_A}{2c^2_W}\frac{\Delta_Z}{1-\Delta_Z}\right)^2\right]. \quad (20)$$

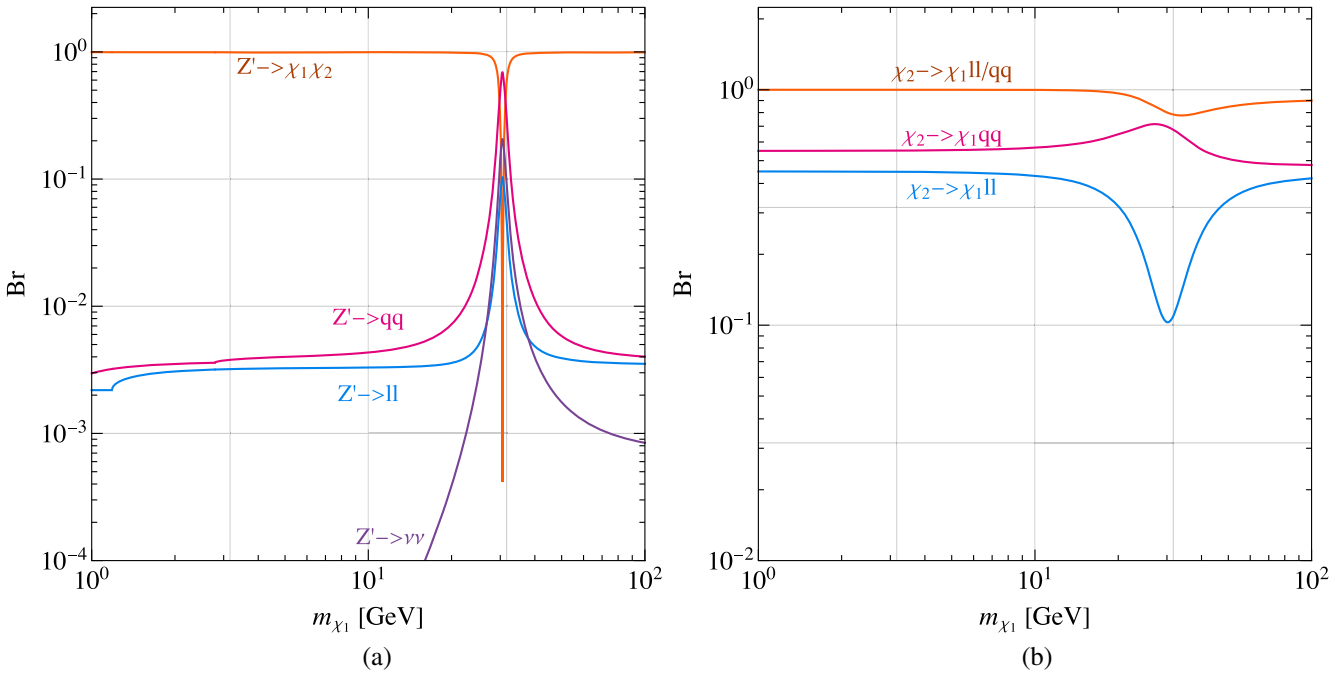


FIG. 1. The decay branching ratio into different final states for the benchmark case of $m_{\chi_1} = 10\Delta_\chi = m_{Z'}/3$, $\alpha_D = 0.1$. Panel (a) shows the Z' case with $\epsilon = 0.1$. Panel (b) shows χ_2 decaying into visible SM finals states.

Here, $\ell = e, \mu$. We find that the lifetime of χ_2 depends on ϵ, Δ_χ, and $m_{Z'}$. Once reducing ϵ or Δ_χ, the lifetime will enhance. The formula can also extend into the final-state jet and neutrino scenarios. Correspondingly, the branching ratios into the visible SM final states are shown in Fig. 1(b). Note that the pole around $m_{\chi_1} \sim 30$ GeV is due to the $m_Z \sim m_{Z'}$. We find that the decay into visible final states (charged leptons and jets) dominates over the neutrino cases. This provides a viable opportunity to conduct the collider signal analysis with visible final states.

III. LEPTON COLLIDER SIGNATURES

In this section, we discuss the production of inelastic DM at the lepton colliders and classify the signal signatures. First of all, the Universal FeynRules Output model file of the inelastic DM model is generated using FeynRules [49], and then we apply MadGraph5_aMC@NLO [50] to generate Monte Carlo events and calculate cross sections for the following signal process:

$$e^+e^- \to Z' + Z/\gamma, \quad Z' \to \chi_2 + \chi_1, \quad \chi_2 \to \chi_1 ll/jj. \tag{21}$$

The Feymann diagram for relevant process is shown in Fig. 2.

In order to conduct the detailed analysis, we adopt the following model parameter benchmarks:

$$m_{\chi_1} = 10\Delta_\chi = m_{Z'}/3, \qquad \alpha_D = \frac{g_D^2}{4\pi} = 0.1. \tag{22}$$

The values are commonly adopted in many studies, as cited in Refs. [13–15,21,26,30]. Therefore, we use them as benchmark examples to illustrate our analysis. Other choices are presented in the Appendix. The χ_1 mass can vary in the range below,

$$m_{\chi_1}/\mathrm{GeV} = (1, 100). \tag{23}$$

This is consistent with the observed DM relic density [13,14,19] for χ_1 as the DM candidate.

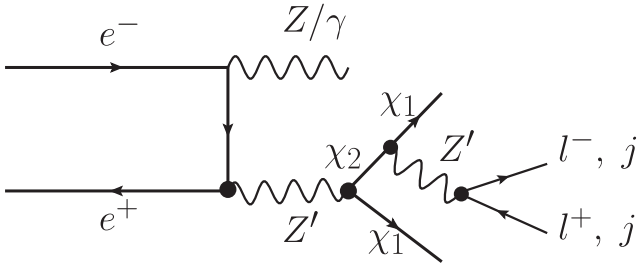


FIG. 2. The Feymann diagram for the processes $e^+e^- \to Z/\gamma + Z', Z' \to \chi_1\chi_2, \chi_2 \to \chi_1 ll/jj$.

Before performing a detailed collider analysis, we first examine the corresponding constraints on the model parameters.

(i) $(g-2)_\mu$: Exchanging Z' at one loop level gives the contribution as

$$\Delta a_\mu = \frac{\alpha_{em}\epsilon^2 m_\mu^2}{\pi m_{Z'}^2} \int_0^1 dx \frac{1}{1 - x + (m_\mu/m_{Z'})^2 x^2} \times [(c_V^\mu)^2 x^2(1-x) + (c_A^\mu)^2(x - x^2)(x-4)]. \tag{24}$$

The most recent measurement of $(g-2)_\mu$ was performed by the Fermilab experiment [51], showing a deviation from the recent SM prediction [52], $a_\mu = (26 \pm 66) \times 10^{-11}$. We choose 2σ errors to place an exclusive limit on the model parameters $\epsilon - m_{Z'}$ in the upper left corner of Fig. 4.

(ii) Electroweak fit: The effects are parametrized by the oblique parameters (STU) [53,54] given by

$$\alpha S = 4\epsilon^2 s_W^2 c_W^2 \frac{1}{1-\Delta_Z}\left(1 - \frac{s_W^2}{1-\Delta_Z}\right),$$
$$\alpha T = -\frac{\epsilon^2 s_W^2}{(1-\Delta_Z)^2}\Delta_Z, \qquad \alpha U = \frac{4\epsilon^2 s_W^4 c_W^2}{(1-\Delta_Z)^2}. \tag{25}$$

The current electroweak fit requires $S = -0.04 \pm 0.10$, $T = 0.01 \pm 0.12$, and $U = -0.01 \pm 0.09$ [2], which can give the upper bound on $\epsilon < 6 \times 10^{-3}$ around Z-boson mass in Fig. 4.

(iii) Collider bounds: Other experimental constraints derive from LEP [53,55], *BABAR* [56], and CMS [57], respectively, as shown in the gray regions of Fig. 4.

(iv) DM abundance: The χ_1 abundance matches the observed DM relic density [13,14,19], which is indicated by the black line. A dimensionless parameter y is defined as

$$y = \epsilon^2 \alpha_D \frac{m_{\chi_1}^4}{m_{Z'}^4}. \tag{26}$$

It uniquely determines the freeze-out annihilation rate by a given parameter combination, frequently adopted in DM abundance analysis [13–15]. Please refer to the Appendix for details.

Now we conduct the detailed collider analysis. The Z' production occurs via $e^+e^- \to Z/\gamma + Z'$ characterized by kinetic mixing parameter ϵ in Eq. (18). Ignoring the masses of the initial electron and positron, we approximately calculate the corresponding cross sections as

TABLE II. The relevant information for different lepton (e^+e^-) colliders, including CLIC [58], ILC [59], FCC-ee [60], and CEPC [61], includes expected center-of-mass energy, integrated luminosity, and detector paramaters. The corresponding profile sketch of the detector components includes the inner tracker, HCAL, and muon chamber (with barrel and end caps) as shown in Ref. [9]. Here, R_e represents incoming radius in the end caps.

			Inner tracker			Muon system					HCAL			
Facility	$\sqrt{s}$ (GeV)	$\mathcal{L}_{lum}$(ab^{-1})	R_I (mm)	R_o (m)	$\pm z$ (m)	R_e (m)	R_I (mm)	R_o (m)	z_I (m)	z_o (m)	R_I (mm)	R_o (m)	z_I (m)	z_o (m)
ILC	250	2	16	1.776	2.212	0.58	4.45	7.755	4.072	6.712	2.058	3.345	2.65	3.937
FCC-ee	91	150												
	160	10	17	2	2	0.35	4.5	5.5	5.5	6.5	2.5	4.5	3	5.5
	240	5												
CEPC	91	100												
	160	6.9	16	1.81	2.35	0.5	4.4	6.08	4.14	5.86	2.058	3.144	2.65	3.736
	240	21.6												

$$\frac{\sigma(e^+e^- \to Z'\gamma)}{\sigma(e^+e^- \to Z\gamma)} \approx 4\epsilon^2 s_W^2 c_W^2 \frac{(c_V^e)^2 + (c_A^e)^2}{(\tilde{g}_V^e)^2 + \tilde{g}_A^e)^2},$$
$$\frac{\sigma(e^+e^- \to Z'Z)}{\sigma(e^+e^- \to ZZ)} \approx 8\epsilon^2 s_W^2 c_W^2 \frac{(c_V^e \tilde{g}_V^e)^2 + (c_A^e \tilde{g}_A^e)^2}{(\tilde{g}_V^e)^4 + \tilde{g}_A^e)^4}. \quad (27)$$

Note that the additional factor of 2 in the second line comes from the final states of identical Z bosons in $e^+e^- \to ZZ$. The subsequent decays of Z' and χ_2 are shown in Fig. 1.

In order to facilitate a more detailed analysis of collider signals, we first elaborate on the different types of lepton colliders, particularly the electron-positron scenario. The particle physics community has actively discussed the possibility of building a new lepton collider to reduce uncertainties and improve precision measurements. Currently, there are two types of proposals for the e^+e^- case: circular and linear colliders, as follows.

(i) CLIC: the Compact Linear Collider [58] with a length ranging from 11 to 50 km and a proposed energy range of (380, 1500, 3000) GeV.
(ii) ILC: the International Linear Collider [59,62] with a length of approximately 20 km and proposed energies of (250, 365, 500) GeV.
(iii) FCC-ee: the Future Circular Collider [60] with a 90 km circular ring and collider energies of (91, 160, 240, 365) GeV.
(iv) CEPC: the Circular Electron-Positron Collider [61,63] with a 100 km circumference and the same energies as the FCC-ee, albeit with smaller luminosities.

Based on the above description and the range of m_{χ_1}, we primarily study the collider signatures for energies below approximately 300 GeV. Furthermore, we focus on investigating the collider signatures for ILC (250 GeV), FCC-ee (91, 160, and 240 GeV), and CEPC (91, 160, and 240 GeV), respectively. Here, the numbers in parentheses represent the collider center-of-mass energies. Correspondingly, the proposed center-of-mass energies, luminosities, and geometrical structures are summarized in Table II. The profile sketch of the detector components of lepton colliders refer to Fig. 3 in Ref. [9].

Since the final states from χ_2 decays involve charged leptons or jets, we will analyze the corresponding collider signatures both individually and in combination. The total signal events $N_{s.e.}$ can be obtained by reconstructing displaced vertices in the above regions using Monte Carlo simulations, as given by

$$N_{\text{s.e.}} = \mathcal{L} \cdot \sigma \cdot \frac{1}{N^{MC}} \sum_{i=1}^{N^{MC}} P_i^{DV} \epsilon_{DV}^i. \quad (28)$$

Here, $\mathcal{L}$ represents the integrated luminosity of the corresponding lepton collider, and σ denotes the cross section for the process $e^+e^- \to \gamma/Z + Z', Z' \to \chi_1\chi_2, \chi_2 \to \chi_1 + \text{vis.}$ N^{MC} is the total number of MC-simulated events. P_i^{DS} is the individual decay probability of the long-lived particle χ_2 in the ith simulated signal event within the respective fiducial component. ϵ_{DV} represents the efficiency of our displaced vertex analysis, which depicts the reconstruction effects, with $\epsilon_{DV} = 100\%$ for simplicity unless otherwise stated [37]. For the details of the Monte Carlo simulations, we use inverse sampling of the decay distribution to simulate the displacement.

As shown in Table II, we consider three distinct detector regions: the interaction point (IP), the muon system (MS), and the hadronic calorimeter (HCAL). Note that the final visible particles from χ_2 decays could either be a pair of charged leptons or jets. In the former case (charged leptons), we consider both the IP and the MS for reconstructing the displaced vertices. In contrast, for jets, we additionally include the HCAL as part of the fiducial volume. Furthermore, the vertex detector and inner tracker for the IP are considered together. The HCAL and MS consist of a barrel and two end caps.

Regardless which of the aforementioned three regions the particle decay occurs in, the visible final states can be detected. Taking into account the Lorentz boost effects, the decay width of χ_2 is

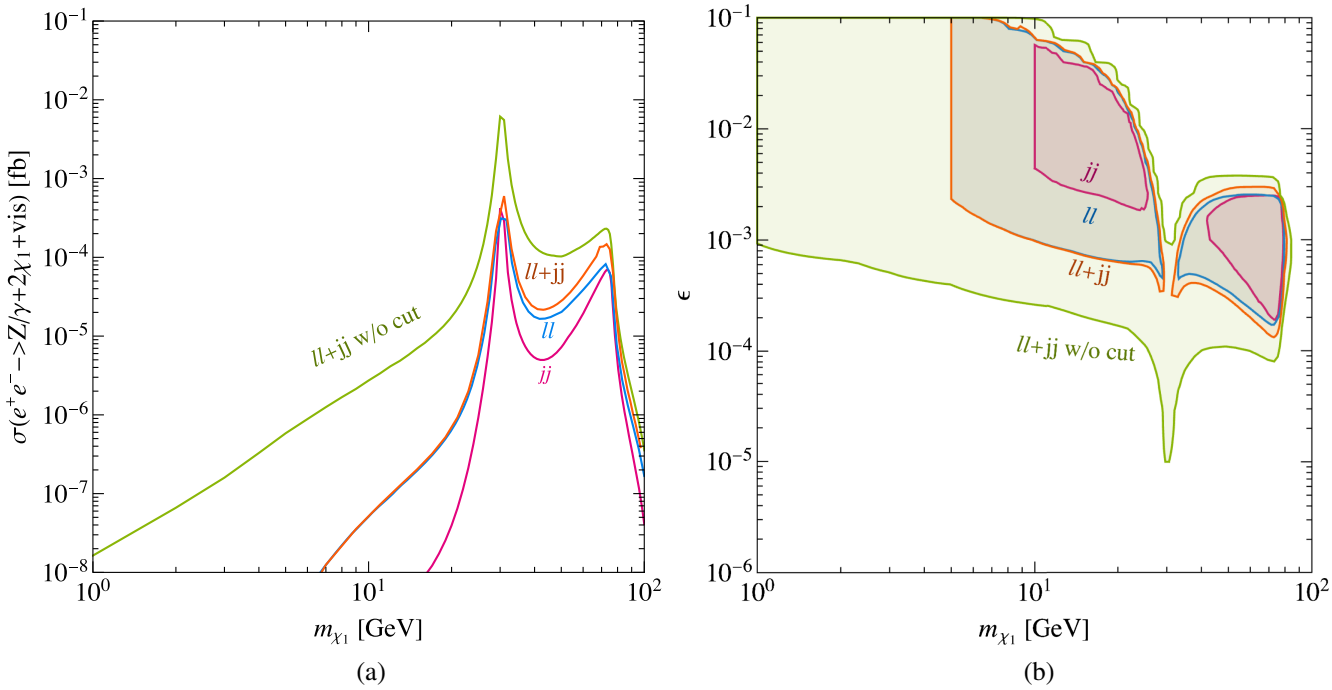


FIG. 3. The cross section $\sigma(e^+e^- \to Z/\gamma + 2\chi_1 + ll/qq)$ and sensitivity on the model parameters for the 240 GeV CEPC. Here we choose the benchmark $m_{\chi_1} = 10\Delta_\chi = m_{Z'}/3$, $\alpha_D = 0.1$. The green represents the visible final states $(ll + jj)$ without the cut. The remaining ones correspond to the cases by imposing a cut in Eq. (30), with magenta for jj, blue for ll, and red for $ll + jj$, respectively. Panel (a) shows the $m_{\chi_1} - \sigma$ plane for fixing $\epsilon = 10^{-4}$. Panel (b) shows the $m_{\chi_1} - \epsilon$ plane for different scenarios.

$$\lambda = \beta_i\gamma_i\tau_{\chi_2} = \frac{p_i}{E_i}\frac{E_i}{m_{\chi_2}}\tau_{\chi_2} = \frac{p_i}{m_{\chi_2}}\tau_{\chi_2}; \tag{29}$$

here, $\beta_i(\gamma_i)$ is the speed (boost) factor of χ_2, and τ_{χ_2} denotes its lifetime. By defining the polar angle between the traveling direction of χ_2 and the z axis as θ_i, we can derive the corresponding selection criteria for observing χ_2 decays within the aforementioned three regions as follows:

(i) IT: $R_I < |\lambda_i \sin\theta_i| < R_o$ and $|\lambda_i \cos\theta_i| < z$
(ii) Barrel: $R_I < |\lambda_i \sin\theta_i| < R_o$ and $|\lambda_i \cos\theta_i| < z_I$
(iii) End caps: $R_e < |\lambda_i \sin\theta_i| < R_o$ and $z_I < |\lambda_i \cos\theta_i| < z_o$

Regardless of the regions in which the decays occur, the visible final-state signals can be detected. Furthermore, to obtain reliable results, we impose the following cuts:

$$p_{tl} > 2.5 \text{ GeV}, \qquad p_{tj} > 5 \text{ GeV}. \tag{30}$$

This corresponds to the requirement that $\Delta_\chi > 5(10)$ GeV for $ll(jj)$ final states.

For convenience, we use the CEPC (240 GeV) as an example to illustrate the analysis details. The relevant results are shown in Fig. 3. Here we choose the benchmark $m_{\chi_1} = 10\Delta_\chi = m_{Z'}/3$, $\alpha_D = 0.1$. Four different scenarios are analyzed, marked with different colors, depending on whether the cuts in Eq. (30) are imposed, and the final states (charged leptons or jets). In Fig. 3(a), the cross section $\sigma(e^+e^- \to Z/\gamma + 2\chi_1 + ll/qq)$ is obtained for $\epsilon = 10^{-4}$ in terms of the DM χ_1 mass m_{χ_1}. We find two distinct peaks around $m_{\chi_1} \sim 30$ GeV and $m_{\chi_1} \sim 80$ GeV. The former case corresponds to $m_{Z'} \sim m_Z \sim 90$ GeV, arising from the interaction coupling pole in Eq. (18). The latter is due to the contribution from $e^+e^- \to \gamma Z'$ induced by $m_{Z'} \sim \sqrt{s}$. Moreover, the cross section for visible final states $(ll + jj)$ without the cuts can reach a maximum of 0.01 fb around $m_{\chi_1} \sim 30$ GeV, as indicated in green. After imposing the cuts in Eq. (30), the corresponding maximum cross section decreases by 1 order of magnitude to 0.001 fb in red, followed by ll in blue and jj in magenta. Additionally, the dominant contribution comes from the charged lepton final states. The corresponding event numbers after imposing the cuts are shown in Table III.

IV. SENSITIVITY

In this section, we discuss the sensitivity of the lepton collider to the model parameters m_{χ_1} and ϵ.

As shown in Fig. 3(b), the sensitivity to the model parameters is analyzed for four distinct scenarios depicted by different colors. We find that the scenario of $ll + jj$ without cuts, marked by the green region, exhibits excellent sensitivity with $O(10^{-3})$, even approaching $\epsilon \sim 10^{-5}$ around $m_{\chi_1} \sim 30$ GeV. Additionally, this scenario ($ll + jj$ without cuts) covers the entire χ_1 mass range. After imposing the cut, the sensitivity region induced by the same

TABLE III. The signal event numbers for different lepton colliders after imposing the cuts. Here we choose the benchmark $m_{\chi_1} = 10\Delta_\chi = m_{Z'}/3$, $\alpha_D = 0.1$.

			Event numbers					
			$\epsilon = 10^{-3}$			$\epsilon = 10^{-2}$		
Facility	$\sqrt{s}$ (GeV)	$\mathcal{L}_{lum}(\mathrm{ab}^{-1})$	$m_{\chi_1} = 10$ GeV	$m_{\chi_1} = 40$ GeV	$m_{\chi_1} = 70$ GeV	$m_{\chi_1} = 6$ GeV	$m_{\chi_1} = 10$ GeV	$m_{\chi_1} = 20$ GeV
ILC	250	2	0.34	0.61	3.12	21.40	56.81	13.89
FCC-ee	91	150	1.77	0	0	79.70	202.22	23.80
	160	10	1.07	5.65	0	81.19	176.29	24.43
	240	5	0.65	1.49	8.44	53.83	139.39	29.41
CEPC	91	100	1.19	0	0	53.66	138.99	20.25
	160	6.9	0.78	4.18	0	56.45	124.27	19.64
	240	21.6	3.10	6.79	38.66	234.02	612.88	142.90

final states narrows down and reduces by 1 order of magnitude for ϵ. Furthermore, the individual scenarios for charged leptons or jets are shown separately. The sensitivity from the charged lepton scenario is significantly superior to that from the jet scenarios, indicating that the dominant contribution to the $ll + jj$ final states comes from the charged lepton case. Therefore, we mainly focus on the case of charged lepton final states for different types of lepton colliders in the following.

The relevant findings are illustrated in Fig. 4, which include both current bounds in light gray regions and the projected lepton collider sensitivity in colored regions. The

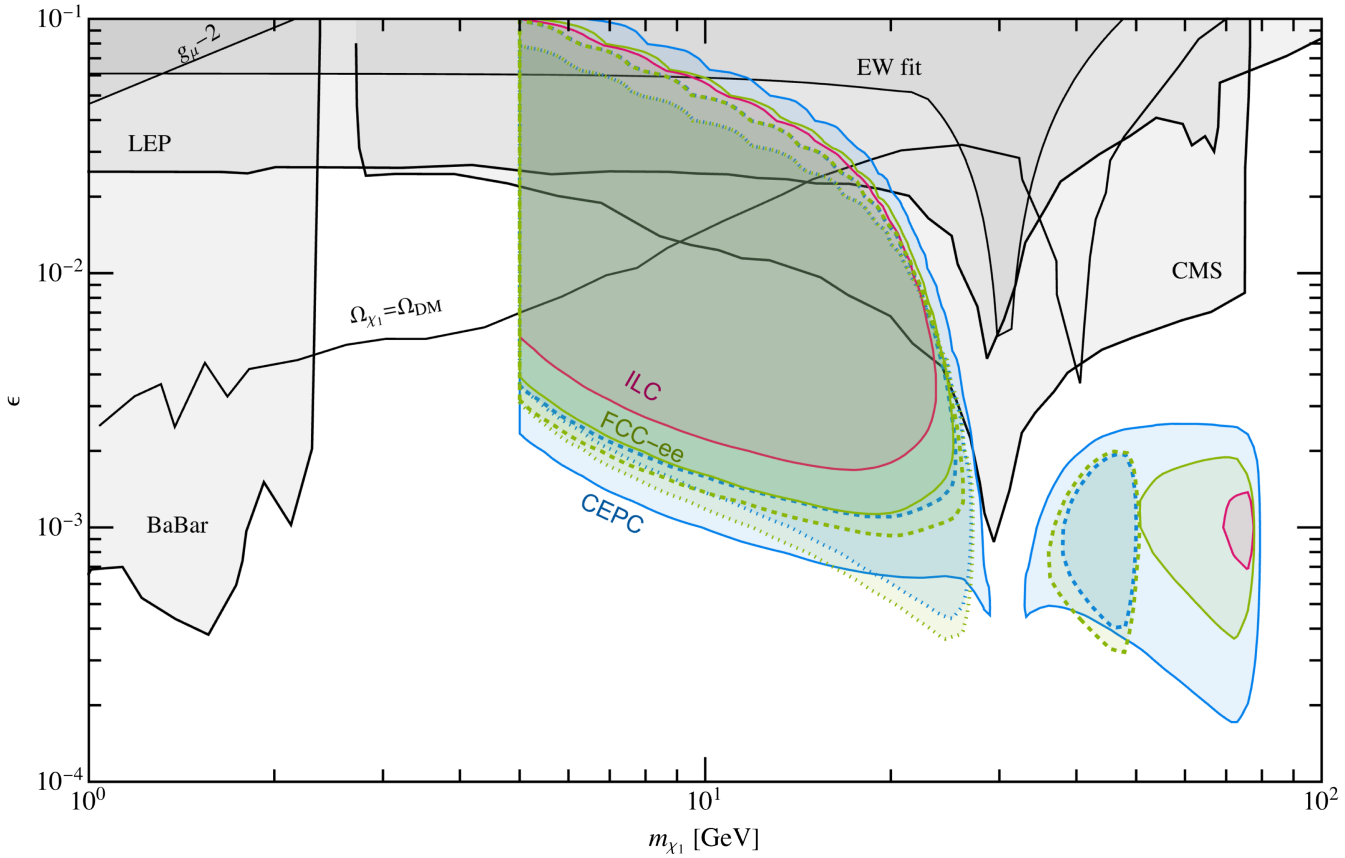


FIG. 4. The current experimental bounds and future lepton collider sensitivities in the $m_{\chi_1} - \epsilon$ plane. Here we choose the benchmark $m_{\chi_1} = 10\Delta_\chi = m_{Z'}/3$ and $\alpha_D = 0.1$. The light gray regions represent the excluded regions from $(g-2)_\mu$ [51,64], electroweak fit [2,54], LEP [53,55], *BABAR* [56], and CMS [57], respectively. The black line represents the region where the abundance of χ_1 matches the observed DM relic density [13,14,19]. Different types of lepton colliders are shown in distinct colors, with the corresponding center-of-mass energy 240/250 GeV (solid), 160 GeV (dashed), 91 GeV (dotted).

gray regions summarize the current experimental constraints as mentioned before.

The colored regions represent the projected sensitivity from different lepton colliders. Our analysis demonstrates that all lepton colliders are capable of probing new parameter regions that are not excluded by current bounds, especially the χ_1 mass regions in (5–28) and (32–80) GeV. Two distinct features are observed, as already mentioned in the previous cross section in Fig. 3(a). First, a kinematic separation emerges near $m_{\chi_1} \sim 30$ GeV, where the χ_2's short decay lifetime (τ_{χ_2}) precludes the possibility of decay within the IT, MS, or HCAL subsystems. When increasing τ_{χ_2} by reducing ϵ, the Z' production rate scales as ϵ^2, leading to significant suppression. Second, an upper mass limit $m_{\chi_1} < 80$ GeV appears when $\sqrt{s} \sim m_{Z'}$, reflecting the kinematic threshold. In addition, distinct performance characteristics emerge across lepton colliders. For CEPC, 240 GeV achieves optimal sensitivity, exceeding 90 and 160 GeV performance, owing to maximal beam energy and enhanced luminosity. Furthermore, CEPC 91 GeV demonstrates unique sensitivity in the (18–26) GeV mass range, whereas the 160 GeV operation exhibits reduced sensitivity primarily due to luminosity constraints. On the other hand, while operating at the same energies, FCC-ee displays marginally different sensitivity profiles due to variations in luminosity and detector acceptance. Each collider energy probes distinct parameter space regions with characteristic sensitivity patterns. Notably, FCC-ee 91 GeV outperforms its 160 and 240 GeV, attributable to superior luminosity conditions. We also find that ILC (250 GeV) has comparatively weaker sensitivity in the majority of intervals, with its coverage fully encompassed by CEPC and FCC-ee at 240 GeV. Combining these projected sensitivities from different lepton colliders, we find that it can approach $\epsilon \sim 2 \times 10^{-4}$ at best, which is clearly advantageous compared to the results from LHC [15,26,30] and Belle [19–21].

V. CONCLUSION

In this work, we investigate the detection prospects for the inelastic dark model with an additional $U(1)_D$ gauge symmetry at various lepton colliders. The new gauge boson Z' from $U(1)_D$ serves as a portal to connect the SM fermions and DM fermions χ. The kinetic mixing ϵ between Z' and the hypercharge field B leads to the Z' production. Also, the Z' interaction with dark fermions $\chi_{1,2}$ further induces the decay chain $Z' \to \chi_1\chi_2$. Here, χ_1 (χ_2) represents the ground (excited) DM fermion, with χ_1 acting as the DM candidate and χ_2 as a long-lived particle, respectively. In order to saturate the observed DM relic density, the mass difference $\Delta_\chi = \chi_2 - \chi_1$ induced by the interaction between the dark Higgs field and the DM sector needs to be small enough, leading to the subsequent decays $\chi_2 \to \chi_1 +$ vis. Based on the sensitivity of Belle and the LHC from previous studies, we explore the projected sensitivity from future lepton colliders, which benefit from cleaner environments and higher luminosities. For the inelastic DM mass m_{χ_1} in the range of (1–100) GeV, we find that the future lepton colliders can probe many unexplored regions beyond current experimental bounds and provide better projected sensitivity than the LHC and Belle, notably for CEPC 240 GeV approaching $\epsilon \sim 10^{-5}$ without cuts. This indicates that the future collider can serve as a complementary tool for exploring the inelastic dark matter model.

ACKNOWLEDGMENTS

W. L. is supported by National Natural Science foundation of China (Grant No. 12205153). J. S. was supported by IBS under Project No. IBS-R018-D1.

DATA AVAILABILITY

No data were created or analyzed in this study.

APPENDIX: DM ABUNDANCE

In the standard thermal freeze-out scenario, the DM abundance today is fixed by the DM number density at the time when its annihilation rate into SM states drops below the Hubble expansion rate. The DM χ_1 relic abundance is governed by Boltzmann equations as

$$\frac{dY_{1,2}}{dx} = -\frac{\lambda_A}{x^2}(Y_1Y_2 - Y_1^{(0)}Y_2^{(0)}) \pm x\lambda_D\left(Y_2 - \frac{Y_2^{(0)}}{Y_1^{(0)}}Y_1\right) \pm \frac{\lambda_S}{x^2}Y_f^{(0)}\left(Y_2 - \frac{Y_2^{(0)}}{Y_1^{(0)}}Y_1\right); \tag{A1}$$

here, $x = m_{\chi_2}/T$ is a dimensionless time variable, and $Y_i = n_{\chi_i}/s(T)$ is a comoving number density normalized to the entropy density $s(T) = 2\pi^2 g_{s,*}T^3/45$ with the number of entropic degrees of freedom $g_{s,*}$. The superscript (0) denotes an equilibrium quantity. $\lambda_{A,S,D}$ are the collision terms from thermally averaged coannihilation, inelastic scattering, and decay processes, respectively, defined by

$$\lambda_A = \frac{s(m_{\chi_2})}{H(m_{\chi_2})}\langle\sigma v(\chi_1\chi_2 \to f\bar{f})\rangle,$$
$$\lambda_S = \frac{s(m_{\chi_2})}{H(m_{\chi_2})}\langle\sigma v(\chi_2 f \to \chi_1 f)\rangle,$$
$$\lambda_D = \frac{\langle\Gamma(\chi_2 \to \chi_1 f\bar{f})\rangle}{H(m_{\chi_2})}. \tag{A2}$$

Here the Hubble rate $H(T) \approx 1.66\sqrt{g_*}T^2/M_{pl}$, where g_* is the number of relativistic degrees of freedom and the Planck mass $M_{pl} = 1.2 \times 10^{19}$ GeV. The decay rates $\Gamma(\chi_2 \to \chi_1 f\bar{f})$ are indicated in Eq. (20), and the relevant

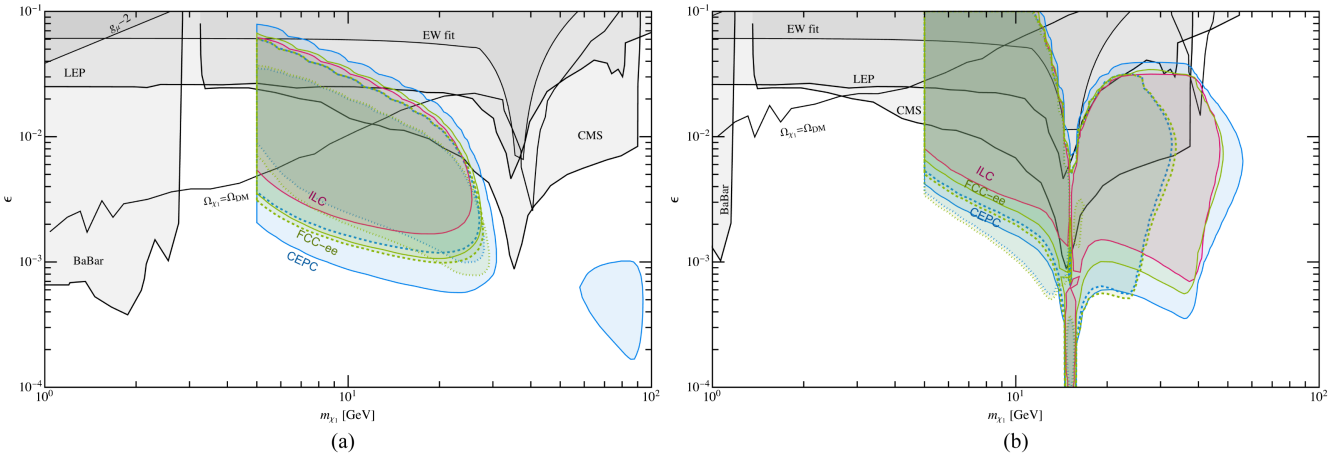


FIG. 5. The same as Fig. 4 for panel (a) $m_{Z'}/m_{\chi_1} = 2.5$ and panel (b) $m_{Z'}/m_{\chi_1} = 6$.

cross sections for the thermal relic abundances are

$$\langle \sigma v(\chi_1\chi_2 \to \bar{f}f)\rangle = \frac{\int_{s_0}^{\infty} ds\sigma(s)(s-s_0)\sqrt{s}K_1\left(\frac{\sqrt{s}}{T}\right)}{8m_{\chi_1}^2 m_{\chi_2}^2 T K_2\left(\frac{m_{\chi_1}}{T}\right)K_2\left(\frac{m_{\chi_2}}{T}\right)},$$
$$\langle \sigma v(\chi_2 e \to \chi_1 e)\rangle \sim 16\pi\epsilon^2 c_W^2 \alpha_{em}\alpha_D \frac{T^2}{m_{Z'}^4}. \tag{A3}$$

Here, $s_0 = (m_{\chi_1} + m_{\chi_2})^2$, and K_1 and K_2 are the modified Bessel functions of the first and second kind. Additionally, in the leading order, the corresponding s-wave coannihilation cross section can be written as

$$\sigma(\chi_1\chi_2 \to \bar{f}f) \approx \frac{4\pi\epsilon^2 c_W^2 \alpha_{em}\alpha_D (m_{\chi_1}+m_{\chi_2})^2}{[(m_{\chi_1}+m_{\chi_2})^2 - m_{A'}^2]^2 + m_{Z'}^2\Gamma_{Z'}^2}$$
$$\propto \epsilon^2\alpha_D \frac{m_{\chi_1}^4}{m_{Z'}^4}\frac{1}{m_{\chi_1}^2} = \frac{y}{m_{\chi_1}^2}. \tag{A4}$$

In the second line, we use the limit of $m_{Z'} \gg m_{\chi_{1,2}}$. For our case of $m_{Z'} > m_{\chi_{1,2}}$, then freeze-out predominantly proceeds through coannihilations $\chi_1\chi_2 \to Z'^* \to f\bar{f}$.

Solving this Boltzmann equation, we obtain Y_1 at freeze-out near $x \sim 20$, which determines the relic abundance as

$$\Omega_{\rm DM} = \frac{\rho_{\chi_1}}{\rho_{\rm cr}} = \frac{m_{\chi_1} s_0 Y_1}{\rho_{\rm cr}} = 0.12h^2, \tag{A5}$$

where the critical density is $\rho_{\rm cr} = 8.1h^2 \times 10^{-47}$ GeV^4, and the present day CMB entropy $s_0 \approx 2969$ cm^{-3}. Therefore, the relevant DM relic density is shown by the black line in Fig. 4.

The corresponding constraints for alternative values of the mass ratio $m_{Z'}/m_{\chi_1}$ are shown in Fig. 5, with $m_{Z'}/m_{\chi_1} = 2.5(10)$ in Fig. 5(a) [Fig. 5(b)]. As the ratio $m_{Z'}/m_{\chi_1}$ increases, the current bounds shift leftward, including the LEP, *BABAR*, CMS, $(g-2)_\mu$, and EW fits, as their bounds are all dependent on the Z' mass. We find that as the ratio $m_{Z'}/m_{\chi_1}$ increases, both the relic density curve and projected sensitivities line shift upward. This shift arises from the correlation between the dark matter relic density and collider signatures. Considering the production and decay processes described in Eqs. (19), (20), and (27) and the long-lived particle χ_2 in Eq. (29), the total event rate scales approximately as $\epsilon^4\alpha_D m_{\chi_1}^4/m_{Z'}^4 = \epsilon^2 y$, where ϵ^2 arises from Z' production, and the remaining terms originate from χ_2 decays. This indicates that increasing $m_{Z'}$ enhances the kinetic mixing, thereby causing both the relic density curve and the projected sensitivity regions to shift upward. Furthermore, a larger mass ratio $m_{Z'}/m_{\chi_1}$ expands the projected sensitivity regions from lepton colliders, particularly at higher values of m_{χ_1}, and the pole feature in Fig. 5(b) appears around $m_{\chi_1} \sim m_{Z'}/6 \approx 15$ GeV, as the small value of Δ_χ^5 in Eq. (20) results in a longer observable lifetime for χ_2.

[1] N. Aghanim *et al.* (Planck Collaboration), Planck 2018 results. VI. Cosmological parameters, Astron. Astrophys. **641**, A6 (2020); **652**, C4(E) (2021).

[2] S. Navas *et al.* (Particle Data Group Collaboration), Review of particle physics, Phys. Rev. D **110**, 030001 (2024).

[3] N. Bernal, M. Heikinheimo, T. Tenkanen, K. Tuominen, and V. Vaskonen, The dawn of FIMP dark matter: A review of models and constraints, Int. J. Mod. Phys. A **32**, 1730023 (2017).
[4] P. Ko, Particle, astroparticle physics and cosmology in dark matter models with dark gauge symmetries, J. Korean Phys. Soc. **73**, 449 (2018).
[5] S. Argyropoulos, O. Brandt, and U. Haisch, Collider searches for dark matter through the Higgs lens, Symmetry **13**, 2406 (2021).
[6] D. Tucker-Smith and N. Weiner, Inelastic dark matter, Phys. Rev. D **64**, 043502 (2001).
[7] S. Antusch, E. Cazzato, and O. Fischer, Displaced vertex searches for sterile neutrinos at future lepton colliders, J. High Energy Phys. 12 (2016) 007.
[8] P. S. Bhupal Dev and Y. Zhang, Displaced vertex signatures of doubly charged scalars in the type-II seesaw and its left-right extensions, J. High Energy Phys. 10 (2018) 199.
[9] K. Cheung and Z. S. Wang, Probing long-lived particles at Higgs factories, Phys. Rev. D **101**, 035003 (2020).
[10] R. Schäfer, F. Tillinger, and S. Westhoff, Near or far detectors? A case study for long-lived particle searches at electron-positron colliders, Phys. Rev. D **107**, 076022 (2023).
[11] K. A. Urquía-Calderón, Long-lived heavy neutral leptons at lepton colliders as a probe of left-right-symmetric models, Phys. Rev. D **109**, 055002 (2024).
[12] Y. Lu, Y.-n. Mao, K. Wang, and Z. S. Wang, LAYCAST: LAYered CAvern Surface Tracker at future electron-positron colliders, arXiv:2406.05770.
[13] E. Izaguirre, G. Krnjaic, and B. Shuve, Discovering inelastic thermal-relic dark matter at colliders, Phys. Rev. D **93**, 063523 (2016).
[14] E. Izaguirre, Y. Kahn, G. Krnjaic, and M. Moschella, Testing light dark matter coannihilation with fixed-target experiments, Phys. Rev. D **96**, 055007 (2017).
[15] A. Berlin and F. Kling, Inelastic dark matter at the LHC lifetime frontier: ATLAS, CMS, LHCb, CODEX-b, FASER, and MATHUSLA, Phys. Rev. D **99**, 015021 (2019).
[16] G. Mohlabeng, Revisiting the dark photon explanation of the muon anomalous magnetic moment, Phys. Rev. D **99**, 115001 (2019).
[17] Y.-D. Tsai, P. deNiverville, and M. X. Liu, Dark photon and muon $g-2$ inspired inelastic dark matter models at the high-energy intensity frontier, Phys. Rev. Lett. **126**, 181801 (2021).
[18] P. Ko, T. Matsui, and Y.-L. Tang, Dark matter bound state formation in fermionic Z_2 DM model with light dark photon and dark Higgs boson, J. High Energy Phys. 10 (2020) 082.
[19] M. Duerr, T. Ferber, C. Hearty, F. Kahlhoefer, K. Schmidt-Hoberg, and P. Tunney, Invisible and displaced dark matter signatures at Belle II, J. High Energy Phys. 02 (2020) 039.
[20] M. Duerr, T. Ferber, C. Garcia-Cely, C. Hearty, and K. Schmidt-Hoberg, Long-lived dark Higgs and inelastic dark matter at Belle II, J. High Energy Phys. 04 (2021) 146.
[21] D. W. Kang, P. Ko, and C.-T. Lu, Exploring properties of long-lived particles in inelastic dark matter models at Belle II, J. High Energy Phys. 04 (2021) 269.
[22] B. Batell, J. Berger, L. Darmé, and C. Frugiuele, Inelastic dark matter at the Fermilab Short Baseline Neutrino Program, Phys. Rev. D **104**, 075026 (2021).
[23] J. Guo, Y. He, J. Liu, and X.-P. Wang, Heavy long-lived coannihilation partner from inelastic dark matter model and its signatures at the LHC, J. High Energy Phys. 04 (2022) 024.
[24] J. Li, T. Nomura, and T. Shimomura, Inelastic dark matter from dark Higgs boson decays at FASER, J. High Energy Phys. 09 (2022) 140.
[25] A. Filimonova, S. Junius, L. Lopez Honorez, and S. Westhoff, Inelastic Dirac dark matter, J. High Energy Phys. 06 (2022) 048.
[26] E. Bertuzzo, A. Scaffidi, and M. Taoso, Searching for inelastic dark matter with future LHC experiments, J. High Energy Phys. 08 (2022) 100.
[27] Y. Gu, L. Wu, and B. Zhu, Detection of inelastic dark matter via electron recoils in SENSEI, Phys. Rev. D **106**, 075004 (2022).
[28] M. Mongillo, A. Abdullahi, B. B. Oberhauser, P. Crivelli, M. Hostert, D. Massaro, L. M. Bueno, and S. Pascoli, Constraining light thermal inelastic dark matter with NA64, Eur. Phys. J. C **83**, 391 (2023).
[29] S. Heeba, T. Lin, and K. Schutz, Inelastic freeze-in, Phys. Rev. D **108**, 095016 (2023).
[30] C.-T. Lu, J. Tu, and L. Wu, Probing inelastic dark matter at the LHC, FASER, and STCF, Phys. Rev. D **109**, 015018 (2024).
[31] J. Liu, L.-T. Wang, X.-P. Wang, and W. Xue, Exposing the dark sector with future Z factories, Phys. Rev. D **97**, 095044 (2018).
[32] S. Amrith, J. M. Butterworth, F. F. Deppisch, W. Liu, A. Varma, and D. Yallup, LHC constraints on a $B-L$ gauge model using contur, J. High Energy Phys. 05 (2019) 154.
[33] F. Deppisch, S. Kulkarni, and W. Liu, Heavy neutrino production via Z' at the lifetime frontier, Phys. Rev. D **100**, 035005 (2019).
[34] F. F. Deppisch, S. Kulkarni, and W. Liu, Searching for a light Z' through Higgs production at the LHC, Phys. Rev. D **100**, 115023 (2019).
[35] W. Liu, K.-P. Xie, and Z. Yi, Testing leptogenesis at the LHC and future muon colliders: A Z' scenario, Phys. Rev. D **105**, 095034 (2022).
[36] K. Asai, A. Das, J. Li, T. Nomura, and O. Seto, Chiral Z' in FASER, FASER2, DUNE, and ILC beam dump experiments, Phys. Rev. D **106**, 095033 (2022).
[37] W. Liu, S. Kulkarni, and F. F. Deppisch, Heavy neutrinos at the FCC-hh in the U(1)B-L model, Phys. Rev. D **105**, 095043 (2022).
[38] J. Li, W. Liu, and H. Sun, Z' mediated right-handed neutrinos from meson decays at the FASER, Phys. Rev. D **109**, 035022 (2024).
[39] W. Liu, F. F. Deppisch, and Z. Chen, Testing leptogenesis and seesaw in the B-L model using long-lived particle searches, Phys. Rev. D **110**, 035017 (2024).
[40] S. K. A., A. Das, G. Lambiase, T. Nomura, and Y. Orikasa, Probing chiral and flavored Z' from cosmic bursts through neutrino interactions, Eur. Phys. J. C **84**, 1224 (2024).

[41] F. F. Deppisch, S. Kulkarni, and W. Liu, Sterile neutrinos at MAPP in the B-L model, arXiv:2311.01719.
[42] W. Liu, S. Kulkarni, and F. F. Deppisch, Revealing the origin of neutrino masses through displaced shower searches in the CMS muon system, Phys. Rev. D **111**, 093003 (2025).
[43] B. Holdom, Two U(1)'s and epsilon charge shifts, Phys. Lett. **166B**, 196 (1986).
[44] B. A. Dobrescu, Massless gauge bosons other than the photon, Phys. Rev. Lett. **94**, 151802 (2005).
[45] R. Foot and X.-G. He, Comment on Z Z-prime mixing in extended gauge theories, Phys. Lett. B **267**, 509 (1991).
[46] K. S. Babu, C. F. Kolda, and J. March-Russell, Implications of generalized Z—Z-prime mixing, Phys. Rev. D **57**, 6788 (1998).
[47] D. Feldman, Z. Liu, and P. Nath, The Stueckelberg Z-prime extension with kinetic mixing and milli-charged dark matter from the hidden sector, Phys. Rev. D **75**, 115001 (2007).
[48] J. Sun and Z.-P. Xing, Dark photon effects with the kinetic and mass mixing in Z-boson decay processes, Phys. Rev. D **109**, 035017 (2024).
[49] N. D. Christensen and C. Duhr, FeynRules—Feynman rules made easy, Comput. Phys. Commun. **180**, 1614 (2009).
[50] J. Alwall, R. Frederix, S. Frixione, V. Hirschi, F. Maltoni, O. Mattelaer, H. S. Shao, T. Stelzer, P. Torrielli, and M. Zaro, The automated computation of tree-level and next-to-leading order differential cross sections, and their matching to parton shower simulations, J. High Energy Phys. 07 (2014) 079.
[51] D. P. Aguillard *et al.* (Muon g-2 Collaboration), Measurement of the positive muon anomalous magnetic moment to 0.20 ppm, Phys. Rev. Lett. **131**, 161802 (2023).
[52] R. Aliberti *et al.*, The anomalous magnetic moment of the muon in the Standard Model: An update, arXiv:2505.21476.
[53] D. Curtin, R. Essig, S. Gori, and J. Shelton, Illuminating dark photons with high-energy colliders, J. High Energy Phys. 02 (2015) 157.
[54] K. Harigaya, E. Petrosky, and A. Pierce, Precision electroweak tensions and a dark photon, J. High Energy Phys. 07 (2024) 201.
[55] A. Hook, E. Izaguirre, and J. G. Wacker, Model independent bounds on kinetic mixing, Adv. High Energy Phys. **2011**, 859762 (2011).
[56] J. P. Lees *et al.* (*BABAR* Collaboration), Search for invisible decays of a dark photon produced in e^+e^- collisions at *BABAR*, Phys. Rev. Lett. **119**, 131804 (2017).
[57] A. Hayrapetyan *et al.* (CMS Collaboration), Search for inelastic dark matter in events with two displaced muons and missing transverse momentum in proton-proton collisions at $s = 13$ TeV, Phys. Rev. Lett. **132**, 041802 (2024).
[58] CLIC Accelerator Collaboration, *The Compact Linear Collider (CLIC)—Project Implementation Plan* (CERN, Geneva, 2018), Vol. 4.
[59] H. Abramowicz *et al.* (ILD Collaboration), The ILD detector at the ILC, arXiv:1912.04601.
[60] A. Abada *et al.* (FCC Collaboration), FCC-ee: The lepton collider: Future circular collider conceptual design report volume 2, Eur. Phys. J. Special Topics **228**, 261 (2019).
[61] W. Abdallah *et al.* (CEPC Study Group Collaboration), CEPC Technical Design Report: Accelerator, Radiat. Detect. Technol. Methods **8**, 1 (2024); **9**, 184 (2025).
[62] T. Barklow, J. Brau, K. Fujii, J. Gao, J. List, N. Walker, and K. Yokoya, ILC operating scenarios, arXiv:1506.07830.
[63] X. Ai *et al.*, Flavor physics at CEPC: A general perspective, arXiv:2412.19743.
[64] S. Borsanyi *et al.*, Leading hadronic contribution to the muon magnetic moment from lattice QCD, Nature (London) **593**, 51 (2021).